Link between b.c.c.–f.c.c. orientation relationship and austenite morphology in CF8M stainless steel

Maxime Mollens, Adrien Guery, Dominique Loisnard, François Hild, Stéphane Roux

Link between BCC-FCC orientation relationship and austenite morphology in CF8M stainless steel

Maxime Mollens,[a,b]* Adrien Guery,[a] Dominique Loisnard,[a]

François Hild[b] and Stéphane Roux[b]

[a] *EDF R&D, Site des Renardières, 77818 Moret-sur-Loing, France, and* [b] *Université Paris-Saclay, CentraleSupélec, ENS Paris-Saclay, CNRS LMPS - Laboratoire de Mécanique Paris-Saclay, 91190 Gif-sur-Yvette, France.*

E-mail: maxime.mollens@edf.fr

Abstract

Slow-cooled CF8M duplex stainless steel is used for critical parts of the primary coolant pipes of nuclear reactors. This steel can endure severe service conditions, but it tends to become more brittle upon very long-term aging (tens of years). Therefore, It is essential to understand its specific microstructure and temporal evolution. As revealed by EBSD analyses, the microstructure consists of millimetric ferritic grains within which austenite lath packets have grown with preferential crystallographic orientations concerning the parent ferritic phase far from former ferrite grain boundaries. Relative to the latter, where the austenite phase is nucleated, the lath morphology and crystal orientation accommodate the two ferrite orientations. Globally, the Pitsch relationship appears to display the best agreement with the experimental data compared to other classical relationships. The austenite lath packets are parallel plate-shaped

laths, characterized by their normal $\boldsymbol{n}$. A novel methodology is introduced to elucidate the expected relationship between $\boldsymbol{n}$ and the crystallographic orientation given the coarse interfaces, even though $\boldsymbol{n}$ is only partly known from the observation surface, in contrast to the 3D crystal orientations measured by EBSD. The distribution of retrieved normals $\boldsymbol{n}$ is shown to be concentrated over a set of discrete orientations. Assuming ferrite and austenite obey the Pitsch orientation relationship, the determined lath normals are close to an invariant direction of the parent phase given by the same orientation relationship.

1. Introduction

It is well established that the macroscopic mechanical behavior of materials is conditioned by their microstructural properties. For instance, the size, shape and texture of crystals in steel and alloys are first order parameters in the prediction of their mechanical response (Kim & Thomas, 1981; Hansen, 2004; Bouquerel *et al.*, 2006; Verma & Taiwade, 2017). In forming processes involving displacive (*i.e.,* diffusionless) transformations, the final texture results from the parent phase texture and the symmetry involved in the displacive mechanisms giving rise to the child phase (Bunge *et al.*, 1984; Bate & Hutchinson, 2000). Similar conclusions are drawn regarding crystal shapes. The child phase morphology is inherited from parent crystal orientations and the induced crystallographic consistency between the two phases. All these observations also hold for alloys with diffusion-controlled transformation, although they have received less attention (Maki *et al.*, 1986; Ameyama *et al.*, 1992; Monlevade & Falleiros, 2006).

Several components of the primary coolant system in nuclear power plants are made of alloys involving complex phase transformation, and they are of fundamental importance to ensure safe operations. In their in-service environment, they undergo severe thermal and mechanical loadings for an extended time duration (Bethmont *et al.*, 1996; Jayet-Gendrot *et al.*, 2000). The temperature they are subjected to leads to slow microstructural transformations resulting in a modification of their mechanical properties. Hence the impact of thermal aging on the risk of failure must be predicted accurately to assess their integrity for long-term operation (Le Delliou & Saillet, 2015). Such materials exhibit a very peculiar dual-phased microstructure formed from an α-ferrite (BCC) to a γ-austenite (FCC) transformation that is responsible for its specific corrosion resistance and resilience properties. This microstructure presents remarkable properties in a broad range of scales from millimetric polygonal parent grains to the atomic scale where thermal aging occurs. When building a consistent multiscale model,

careful investigations of the microstructure are to be carried out. Understanding its dual-phase layout and crystallographic relationships is required to control the deformation mechanisms occurring during the component lifetime. At first sight, both should be deduced from the crystallographic orientation relationship (OR) between the two phases, based on prior knowledge of the parent phase. Numerous and rigorous experimental and numerical works have proven the link between ORs, crystallographic properties and morphology in martensitic steels in which displacive transformation (from γ-austenite to α-ferrite) occurs. Morito *et al.* (Morito *et al.*, 2006) have listed a series of historical works on this issue, and more recent studies continue to tackle the complex mechanisms of martensite transformation with interpretation of experimental observations (Baur *et al.*, 2019; Ramachandran *et al.*, 2020) and numerical simulations (Engin & Urbassek, 2008; Tateyama *et al.*, 2008; Malik *et al.*, 2012; Zhang *et al.*, 2021). Materials with diffusion-controlled transformations were also studied but to a much lesser extent (Ameyama *et al.*, 1992; Weatherly & Zhang, 1994). The literature discussing such transformations often considers synthetic materials having microstructures differing significantly from that of industrial duplex stainless steels used in primary cooling circuits. The strain resulting from γ-austenite to α-ferrite transformation cannot be accomodated by diffusion only and plastic strain thus occurs. Additionally, the slow cooling carried out to reach desired microstructural properties favors gradual transformation with elemental partitioning and ultimately local lattice parameter changes (Self *et al.*, 1981). These factors forbid the recourse to historical microscopy tools and models to perform an accurate analysis of transformation strain and product morphology. Hence, it is necessary to develop an experimental method that provides crystallographic measurements and their statistics to describe the microstructure at the scale of industrial components. In this respect, very high accuracy is not critical because of the intrinsic variability of the local microstructure, but a statistical representativity is

sought. The links between crystal orientation and morphology as well as the description of the spatial distribution of the two phases are the first steps in a strategy aiming at proposing a microstructure-based constitutive model.

Tools commonly used for an accurate determination of crystallographic parameters may not be suitable for the slowly cooled duplex microstructure microstructure. In particular, transmission electron microscopy is not appropriate as its characterization cannot safely be scaled up to reach the characteristic scale of the grains. Consequently, mostly Electron BackScattered Diffraction (EBSD) analyses will be used in this paper as they allow for generating the statistics needed to move on to higher scales.

The outline of the paper is as follows. First, material characteristics and experimental characterization methods are described in Section 2. Observations regarding the specific microstructural properties are extracted from EBSD measurements in Section 3. To address the complexity associated with the material history, a specific post-processing of EBSD maps is introduced for determining preferential directions of austenite (Section 4). The results are then confronted to the ultimate accuracy reachable with such approaches. Last, the previously reported observations are discussed in Section 5 together with perspectives toward future studies.

2. Experimental Procedures

The studied material is a cast duplex CF8M stainless steel. The samples were taken from an 80 kg cast ingot ($\approx$ 6.4 dm^3) using electrical discharge machining (EDM) far from external surfaces to avoid inhomogeneous zones. The ingot was cast, then air-cooled for approximately 15 days before being heat-treated to 1120°C for 6 h and 20 min, and then water-quenched. The composition is given in Table 1 for the major chemical components. For SEM observations and EBSD acquisitions, the samples were mechanically polished up to 0.1 µm grain size and then processed with an oxide pol-

ishing solution. Acquisitions were carried out on a Mira3 SEM from TESCAN using an accelerating voltage of 30 kV. 120 × 120 pixels diffraction patterns were imaged on a phosphor screen and captured on a CCD camera provided by Nordif. The indexation was performed with "OIM Data Collection" software using the standard Hough transform method. All EBSD maps had a 3 µm step size. The open source Matlab MTEX toolbox (Bachmann *et al.*, 2010) was used for its very convenient and flexible plotting features. Since only cubic structures (corresponding to the $m\bar{3}m$ Laue group) are discussed in the following, all classical EBSD maps are colored using a standard inverse pole figure (IPF) color coding using sample normals $\boldsymbol{z}$ as a reference. The maps coordinates always coincide with the crystallographic orientation reference system. These maps are abbreviated to "IPF-Z" for convenience.

In terms of the volume of data required to extract a statistical description of the microstructure, seven samples taken from different positions in the ingot core were characterized. A 2 × 10 mm^2 map has been acquired for each sample. A total surface area of 140 mm^2 was mapped, which is an order of magnitude larger than the largest microstructure features described in the following.

Table 1. *Measured chemical composition (wt.%) of the ingot from which samples were extracted.*

C	Si	Mn	S	P	Cr	Ni	Mo	Cu	Co
0.032	1.04	0.80	0.0007	0.025	20.9	10.4	2.68	0.17	0.02

3. Observations

The material obtained from the casting process has two phases resulting from the partial ferrite to austenite transformation, and the solutionizing heat treatment recovering some of the transformed ferrite during the first cooling step. The analyzed specimens have roughly a 25/75 vol.% ratio for ferrite and austenite, respectively. The resulting microstructure is shown in Figure 1. The orientation map of the α-phase reveals the geometry of primary grains with distinct areas of uniform orientation. Insofar as the

ingot is thick, the cooling slow and the samples taken far from the edges, these areas can be considered as resulting from equiaxed grains of random crystallographic orientations. Thus, there is no specific sample symmetry inherited from the casting process. Conversely, the γ-phase exhibits elongated lath colonies within which crystallographic orientations are homogeneous or smoothly varying.

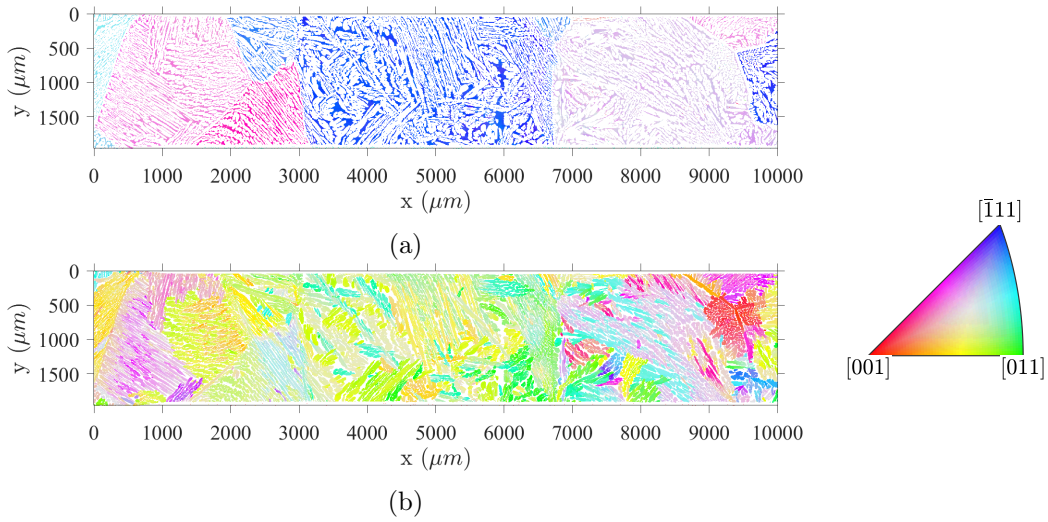

Fig. 1. Microstructure of CF8M duplex stainless steel represented by an IPF-Z map. (a) α-phase map displaying large ferritic grains resulting from the first phase transformation. (b) Austenitic lath network growing within ferritic grains.

3.1. Primary ferrite grain inner structure analysis

In order to quantify possible links between parent and child orientations, and their correlation with the laths morphology, it is necessary to first estimate the primary phase orientation where laths have grown from. The remaining α-phase is then utilized to recover the primary grain geometry using, for instance, a crystallographic orientation based inpainting process (Mollens *et al.*, 2022). The recovered orientation map displays millimeter-size polygonal grains resulting from the first phase transformation (*i.e.,* liquid to solid). Hence, at each pixel coordinate $\boldsymbol{x}$ of the map, the austenite orientation $\boldsymbol{g}_\gamma(\boldsymbol{x})$ can be connected to its parent phase orientation $\boldsymbol{g}_\alpha(\boldsymbol{x})$ (*i.e.,* the misorientation

$\boldsymbol{m}(\boldsymbol{x}) = \boldsymbol{g}_{\alpha}^{-1}(\boldsymbol{x})\,\boldsymbol{g}_{\gamma}(\boldsymbol{x})$ is measured).

Commonly mentioned orientation relationships (ORs) in BCC $\leftrightarrow$ FCC phase transformation include Bain (B) (Bain & Dunkirk, 1924), Kurdjumov-Sachs (KS) (Kurdjumow & Sachs, 1930), Nishiyama-Wassermann (NW) (Nishiyama, 1934; Wassermann, 1935), Pitsch (P) (Pitsch, 1959) and Greninger-Trojano (GT) (Greninger & Troiano, 1949). Experimentally, measured ORs are more than 9° away from B, and most of the time related to either KS or NW (Verbeken *et al.*, 2009). These two ORs actually result from experimental observations using X-ray diffraction in the FCC $\rightarrow$ BCC case. P and GT ORs were identified using transmission electron microscopy (TEM) approximately 20 years later. Some authors mentioned that ORs in BCC $\rightarrow$ FCC transformations were far less discussed even if some relatively recent studies on meteorites (Bunge *et al.*, 2003; He *et al.*, 2006; Nolze, 2008; Yang *et al.*, 2010) and various metallic alloys (Stanford & Bate, 2005; Fukino *et al.*, 2011; Rao *et al.*, 2016; De Jeer *et al.*, 2017; Haghdadi *et al.*, 2020; Cai *et al.*, 2021) have appeared.

ORs are defined by the set of parallel planes and directions given in Table 2. Then, the misorientation is the rotation that maps the crystal directions $\boldsymbol{d}_{\alpha}$ of the child phase to their parallel relatives $\boldsymbol{d}_{\gamma}$ in the parent frame. The misorientation obeying $\boldsymbol{d}_{\gamma}^{1} || \boldsymbol{d}_{\alpha}^{1}$ and $\boldsymbol{d}_{\gamma}^{2} || \boldsymbol{d}_{\alpha}^{2}$ is such that $\boldsymbol{d}_{\gamma}^{1} = \boldsymbol{m}_{\alpha\rightarrow\gamma}\boldsymbol{d}_{\alpha}^{1}$ and $\boldsymbol{d}_{\gamma}^{2} = \boldsymbol{m}_{\alpha\rightarrow\gamma}\boldsymbol{d}_{\alpha}^{2}$. The axis-angle representation of the misorientation associated with the parallelism conditions is given in Table 2. It is worth noting that a definition of the orientation relationship based on a misorientation only is somewhat reductive since a non-zero strain is needed to accommodate the crystal atomic spacing.

Table 2. *Orientation relationships commonly referenced between FCC and BCC lattices. Both parallelism conditions and axis-angle pairs are given. The latter corresponds to the pair having the smallest rotation angle of all the symmetrically equivalent operators*

OR	Plane	Direction	angle/axis pair
Bain	$(001)_\gamma \parallel (001)_\alpha$	$[110]_\gamma \parallel [100]_\alpha$	45.0° / [0 0 1]
KS	$(111)_\gamma \parallel (110)_\alpha$	$[\bar{1}10]_\gamma \parallel [\bar{1}11]_\alpha$	42.9° / [0.97 0.18 0.18]
NW	$(111)_\gamma \parallel (110)_\alpha$	$[\bar{1}10]_\gamma \parallel [001]_\alpha$ $[11\bar{2}]_\gamma \parallel [\bar{1}10]_\alpha$	46.0° / [0.20 0.98 0.08]
P	$(110)_\gamma \parallel (111)_\alpha$	$[001]_\gamma \parallel [\bar{1}10]_\alpha$ $[\bar{1}10]_\gamma \parallel [11\bar{2}]_\alpha$	45.0° / [0.08 0.20 0.98]
GT	$(111)_\gamma \parallel (110)_\alpha$	$[\overline{12}, 17, \bar{5}]_\gamma \parallel [\overline{17}, 17, 7]_\alpha$	44.2° / [0.97 0.19 0.13]

Data obtained from a single ferritic grain are shown in Figure 2. Figure 2(a) displays austenite orientations (colored using the standard inverse pole figure code for cubic symmetry) grouped in lath packets with uniform or smoothly varying crystal orientations. These packets are also characterized by a preferred morphology. The comparison with all symmetrically equivalent child orientations (*i.e.,* so-called variants) predicted for KS (Figure 2(b)) and the distance distributions with some reference ORs in Figure 2(c) highlights the scatter of crystal orientations.

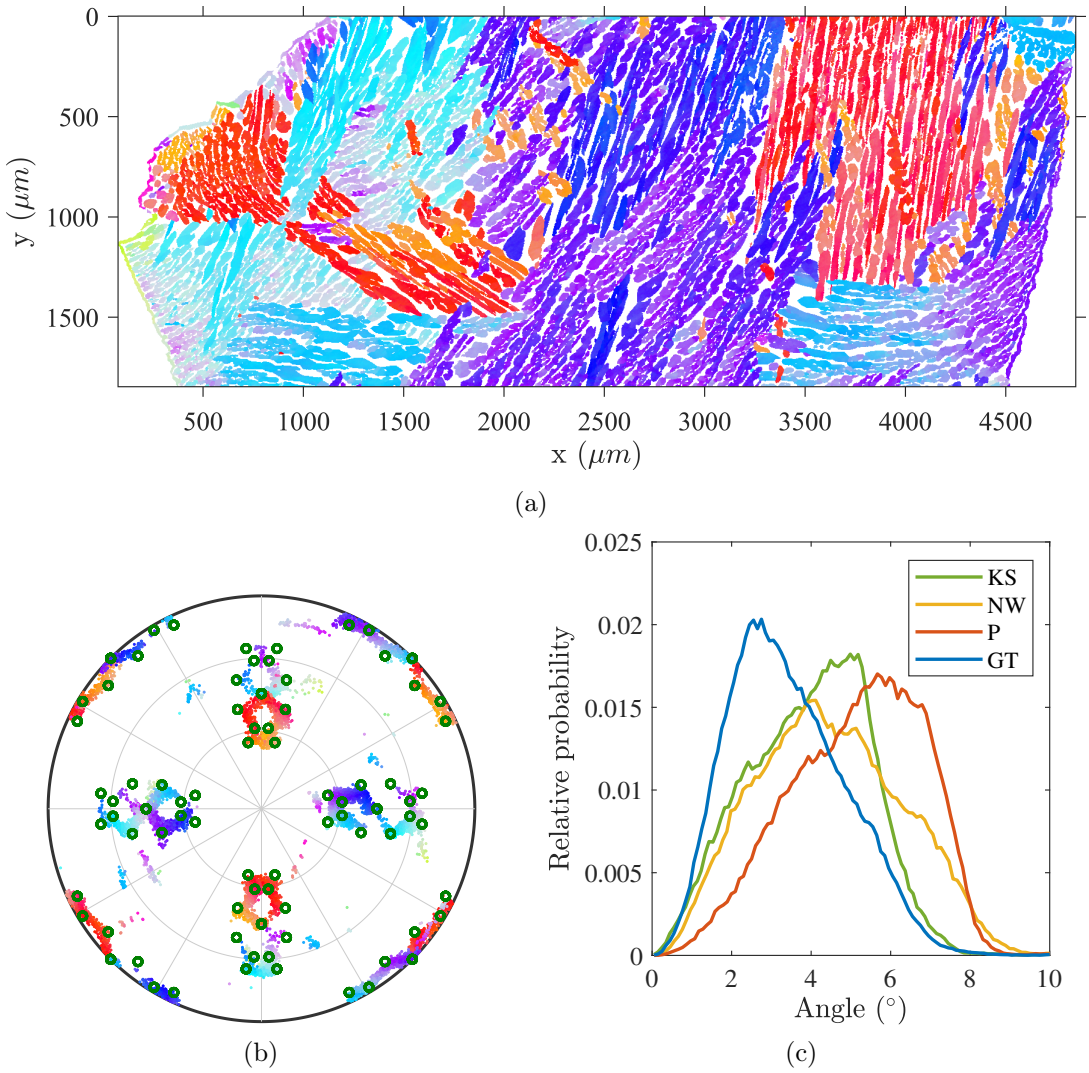

Fig. 2. Austenite orientation in a single ferritic grain. (a) IPF-Z map. (b) [111] pole figure in the ferrite crystallographic frame displaying the γ-orientation spread in a single ferritic grain. The orientations are colored using the IPF-Z color coding convention to relate to sub-figure 2(a). The exact KS variants are plotted in green to emphasize the continuity of observed OR. Only 1% of measured points of the data present on the spatial map is shown in the pole figure. (c) Histograms of rotational angle to the closest variant for four classical ORs in FCC $\leftrightarrow$ BCC systems showing that there is not a single representative OR in the CF8M alloy.

The most discussed cases of orientation spread around common ORs involve martensitic steels (Nolze & Geist, 2004; Cayron *et al.*, 2010; Yardley & Payton, 2014; De Jeer *et al.*, 2017; Hayashi *et al.*, 2020). Their origin is still discussed (Bhadeshia, 2011; Cay-

ron *et al.*, 2011; Hayashi *et al.*, 2020) and displacive mechanisms are not expected in the present case because of the very low cooling rate after casting and the long solutionizing process. Instead, significant freedom is given to diffusion mechanisms is given during the ingot manufacturing. The rotational distance to distinct ORs is then presumably associated with an accomodation to minimize the interfacial energy during precipitate growth following an edge-to-edge sympathetic nucleation process (Ameyama *et al.*, 1992).

The microstructure of interest presents visible characteristics that differ from diffusion-controlled microstructures studied in the literature. For instance, α-γ stainless steels studied by Maki *et al.* (Maki *et al.*, 1986), Ameyama *et al.* (Ameyama *et al.*, 1992) and Haghdadi *et al.* (Haghdadi *et al.*, 2018; Haghdadi *et al.*, 2020) displayed a high density of both intragranular and boundary nucleated precipitates. A fundamental difference with CF8M alloy is the resulting spatial distribution of child nuclei. The reference materials had a large amount of retained parent phase (around 50%) and a large amount of child variants is present in each parent grain. The characterized CF8M microstructure appears much closer to the α-β microstructure of brass characterized by Stanford and Bate (Stanford & Bate, 2005) in the sense that the forming conditions had promoted the growth of large, millimetric, parent grains inside which a few number of child variant clusters were present. There is also a strong similarity in the variety of morphologies, from globular to sharper-shaped laths, with this Cu-Zn alloy that is missing in the previously mentionned steels. Additionally, all lath clusters seem to have grown from a small number of nuclei forming at former ferritic grain boundaries. This is to be contrasted with Ameyama *et al.* (Ameyama *et al.*, 1992) who observed a dense array of child nuclei at parent grains boundaries.

Moreover, locally measured OR in a single cluster may vary over a long characteristic length along with morphological changes. This morphological "gradient" is rather linked

to a transition between OR variants than to statistical dispersion with respect to a fixed OR. A specific post-processing procedure of orientations was developed to reveal this aspect. Instead of considering the crystallographic distance over the symmetry group, it was chosen to rely on an image-processing based interpretation of the distribution of OR variants. Stereographic projections normal to the principal cubic directions of these variants show a nearly circular pattern (Figure 3(a)) from which the approximate expression "Bain circles" originates. Knowing the Bain circle (*i.e.,* Bain variant) on which lies an experimental γ-orientation $\boldsymbol{g}_{child}$, according to its parent α-orientation $\boldsymbol{g}_{parent}$, one may parameterize the angular position θ of $\boldsymbol{m} = \boldsymbol{g}_{parent}^{-1} \cdot \boldsymbol{g}_{child}$ (*i.e.,* associated misorientation) on a circle centered about the Bain variant (Figure 3(a)). This step was achieved by projecting the quaternion vector representing $\boldsymbol{m}$ onto the plane normal to the Bain variant, and computing its polar angle with respect to an arbitrary direction. Hence, knowing $\boldsymbol{g}_{parent}$ allows one to reduce the description of $\boldsymbol{g}_{child}$ to two parameters, namely, the Bain variant and θ. The angle θ computed for austenitic orientations shown in the ferritic grain of Figure 2(a) is plotted on a [100] spherical projection in Figure 3(b).

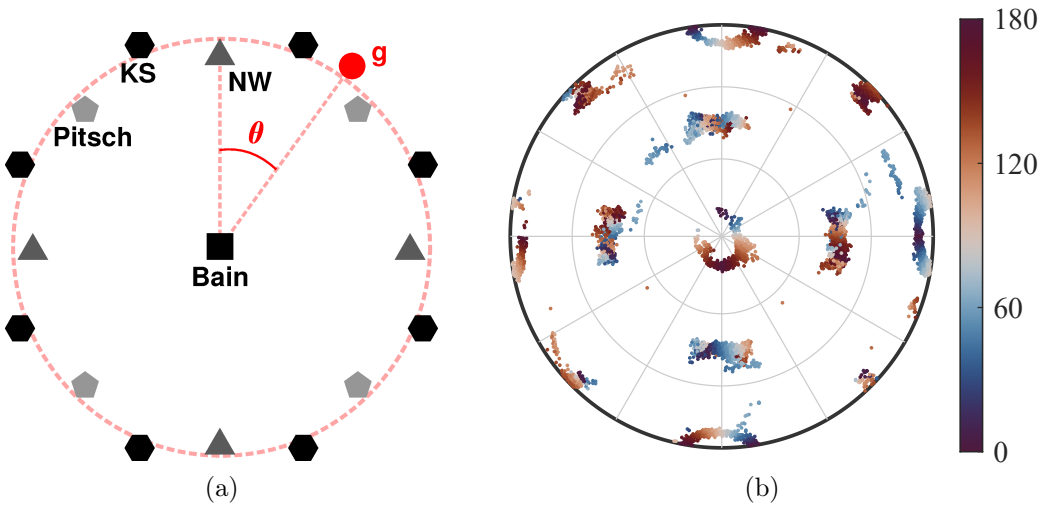

(a) (b)

Fig. 3. Parameterization of γ-orientations according to their distribution about their corresponding Bain variant in a single primary ferrite grain. (a) Schematic representation of θ parameterization for a single Bain variant. The angle is taken between the orthogonal projection $\boldsymbol{g}$ and an orthogonal vector taken among three basis vectors of the ferrite grain crystallographic frame. Thus, only the θ variation is indicative of a distribution of orientations around Bain groups. (b) [100] pole figure of γ-orientation in the α-grain reference frame. Orientations are colored according to the value of θ.

Interestingly, the "circles" observed from the present EBSD analysis and shown in Figure 3(b) display a quasi continuous distribution about each Bain variant. As shown in Figure 4(a), many different laths are encountered around each Bain variant, at different (but close) specific distances to Bain OR. The θ parameterization depicted in Figure 4(b) reveals an important feature of the γ-orientation distribution. In the ferrite reference frame, the continuous orientation around Bain circles correlates well with their morphology as observed on spatial maps. In some Bain groups (delimited by black lines on the spatial maps), the θ range is close to 180°, which reflects a transition from a near horizontal lath shape to a near vertical lath shape on the 2D section given by the EBSD maps. A 180° θ range also means that multiple ORs are crossed around a Bain group. In other words, a single spatial Bain group may contain multiple variants of a single OR, smoothly connected through progressive orientation changes at the

maps scale. The θ-parametrization is only relevant for orientations lying on (or close to) the Bain circles, considering a sensible tolerance regarding the EBSD measurement accuracy. In this example, a small number of regions is far from all Bain variants (distance greater than 15° in Figure 4(a)). They result from the phase transformation mechanisms during cooling, and more specifically from phenomena occurring at primary ferritic grain boundaries that are detailed in the following section.

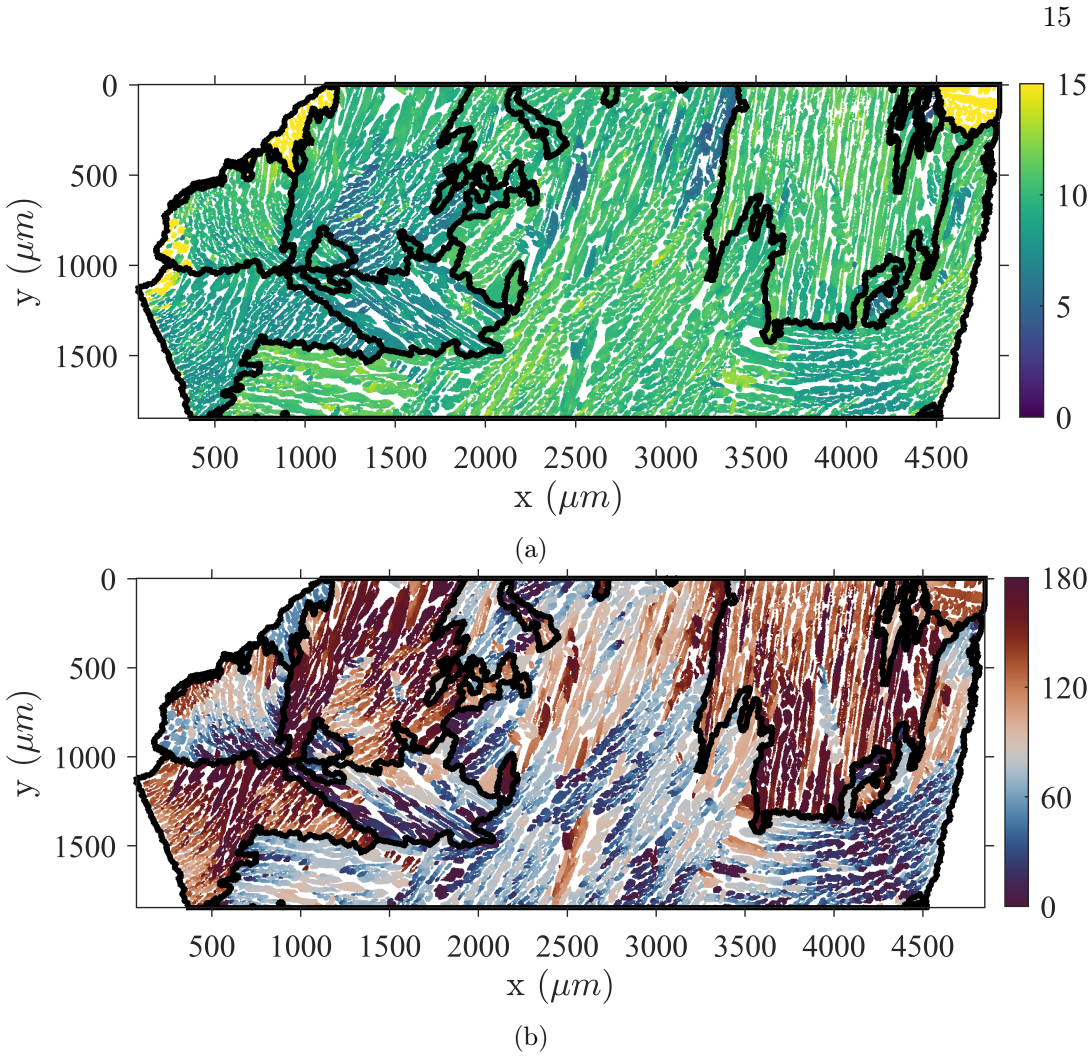

Fig. 4. Illustration of the variant crossing phenomenon. (a) Crystallographic distance (in degrees) to Bain OR. Frequently reported KS and NW ORs are at 11.07° and 9.74°, respectively. The map exhibits a much broader scatter. The black boundaries delineate different Bain groups. (b) Spatial map colored according to the value of θ. This sub-figure shows that the orientation may cross multiple variants of a given OR in a single Bain group while preserving a spatial continuity at this scale (*i.e.*, θ varies much more than 7.54°, which is the smallest $\Delta\theta$ separating two variants in the cited ORs.

3.2. Primary ferrite grain boundaries neighborhood analysis

The spatial orientation maps allow one to propose a schematization of austenite nucleation and growth steps. The surfaces describing primary ferritic grain boundaries are first replaced by a "thickened" austenitic surface with the same primitive shape.

The nucleation giving rise to these films starts at grain junctions. This observation is supported by the EBSD maps on which austenite nuclei seem to appear nearly simultaneously at multiple triple points until they meet on the former boundary as a result of the growth kinetics. This observation means that the austenite film around a single ferritic grain is not monocrystalline. Additionnally, the child orientation at a junction presumably results from a variant selection mechanism with a *single* grain. Considering that typically four randomly oriented grains meet at a junction in the bulk, a child orientation cannot accurately follow an OR with all of them. The orientation maps reveal that the child nuclei orientation is linked to a single parent grain only and that these orientations are kept by laths growing inside the grains even though no OR is followed with most of them.

Since lath packets grow from former ferritic grain boundaries, the latter is classified into two categories. *Almost-coherent* boundaries (*i.e.,* low angle grain boundaries) and *incoherent* boundaries where the disorientation is high (more than 10°). In almost-coherent boundaries, Bain groups from both sides of the boundary are close or may cross each other. Consequently, there is a good agreement between orientations in both grains hinting that, at the present scale, the laths are crossing the original ferrite grain boundary. Figure 5 shows such an example. With a disorientation angle of 6.86° between the two ferritic grains, the morphology and crystal orientations are preserved on both sides of the boundary. The pole figures in Figure 5(b,c) illustrate the small gap between the two sides given the accuracy of orientation measurements. More importantly, they demonstrate that in each grain, austenite orientations lie on the Bain circle given by its ferrite orientation, meaning that a slight rotation occurs in the vicinity of the boundary to comply with this observation.

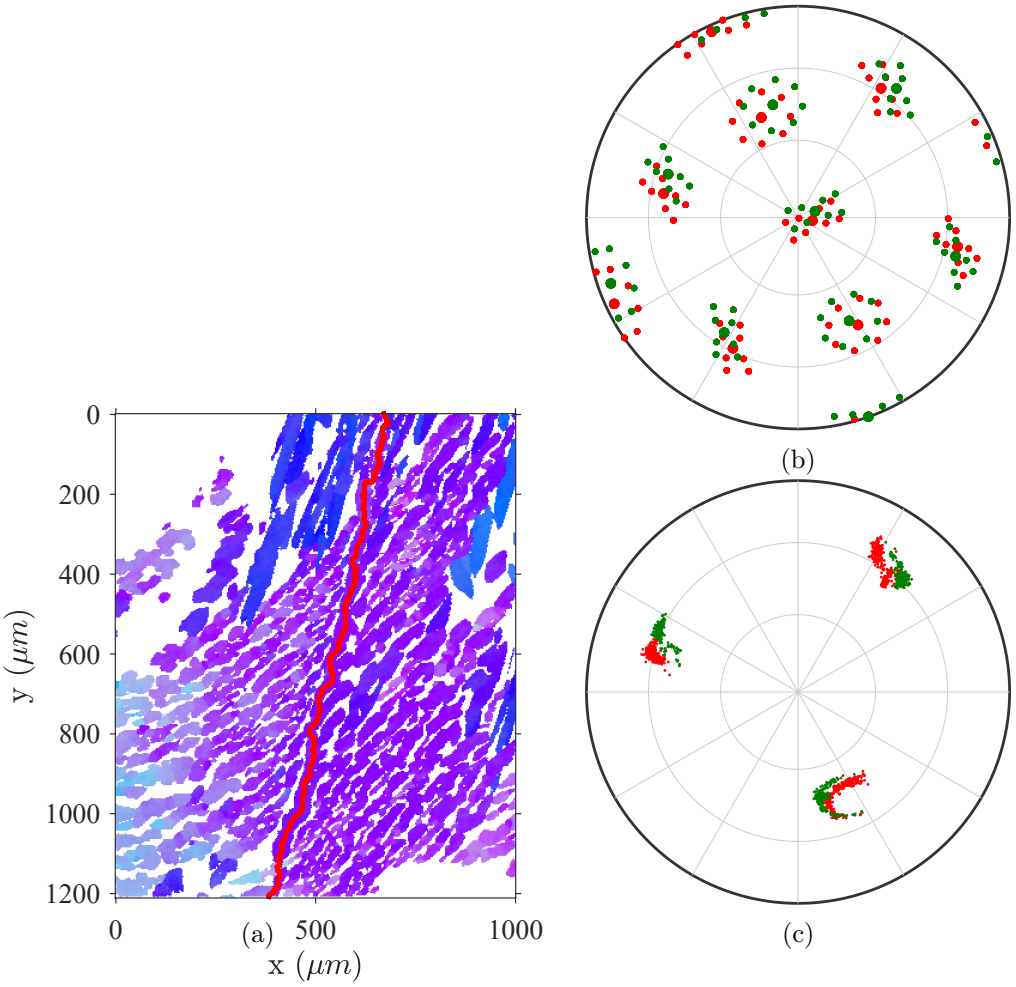

Fig. 5. Orientation and morphology for an almost-coherent grain boundary. (a) IPF-Z map. The primary α-grain boundary is plotted in red. Morphology and orientation of austenite appear similar on either side of the boundary. (b) [100] pole figure of the simulated KS and B variants given the primary α grain orientations. The red points correspond to the left grain, and green to the right one. (c) [100] pole figure showing actual γ-orientations measured in both grains using the previous color coding.

The second type of boundaries, referred to as incoherent, corresponds to a large disorientation angle boundary illustrated in Figure 6(a). Since the child phase predominantly starts growing from these boundaries, severe accommodation should occur to grow on the side where its orientation does not lie on the corresponding Bain group. Yet, the crystallographic orientation is preserved across such boundaries at the cost of a loss of coherence with the parent lattice. Figure 6(b) corresponds to the predicted

[100] directions according to Bain and KS ORs for the two parent grains. Figure 6(c) reveals the actually measured [100] directions being far from the predicted ones for the top grain (red points in Figure 6(b,c)) and more coherent with the Bain zone predicted for the bottom grain. However, in the incoherent grain, austenite takes the shape of laths with a different morphological orientation possibly adapted to the top grain orientation.

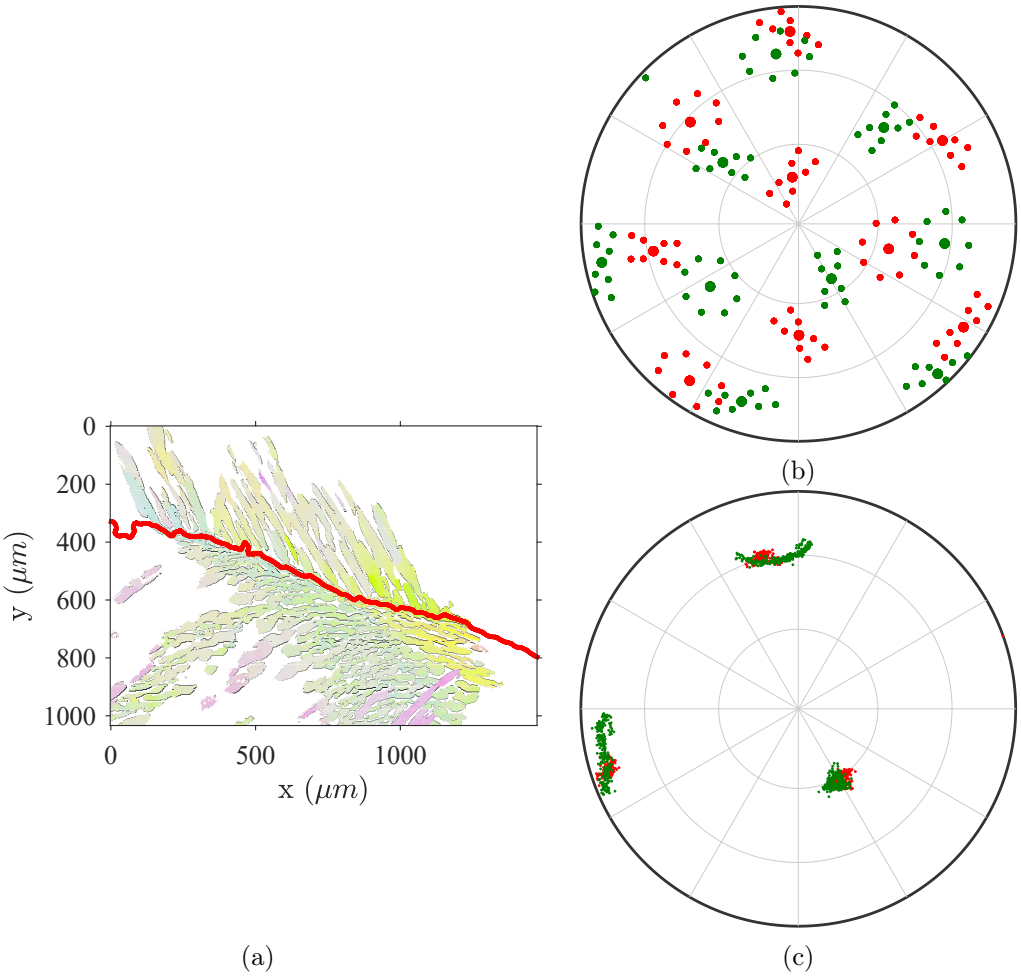

Fig. 6. Orientation and morphology for an incoherent boundary. The disorientation between the two primary α-grains is 41.1°. (a) IPF-Z map. The primary α-grain boundary is plotted in red. The crystallographic orientation is preserved on both sides of the boundary. In the incoherent grain, a lath shape is also preserved with a different morphological orientation. (b) [100] pole figure of the simulated KS and B variants given the primary α-grain orientations. The red points correspond to the bottom grain, and green to the top one. (c) [100] pole figure showing the preservation of γ phase orientations in the two parent grains even if it is far from a stable configuration given by standard ORs.

4. Lath plane determination

4.1. Method

The determination of the plane of lath-shaped austenitic crystals (*i.e.,* the so-called habit plane) is of great interest to study the local mechanical behavior. Lath clusters have near uniform or smoothly varying crystallography and morphology. Assuming that these orientations result from a unique mechanism linked to preferential growth directions, there must exist a limited number of configurations to which a relevant homogenized mechanical behavior may be attributed. However, if austenite lath packets are large, their boundaries locally display large fluctuations. This property is likely to be inherited from the long solutionizing heat treatment and prevents from using the standard habit plane determination methods associated with TEM measurements (Ameyama *et al.*, 1992; Okamoto & Oka, 1992; Zhang *et al.*, 1995; Luo & Liu, 2006), requiring an accurate and unbiased definition of phase boundaries. Therefore, one may only rely on average measurements to determine the laths extension.

The lath plane orientation in 3D is fully described by the orientation of its normal vector. However, as only cross-sections with the observation plane are accessible, they cannot provide the 3D lath orientation. Figure 7 illustrates the ill-posedness of a direct evaluation of the lath plane normal. However, assuming a unique link between the orientation of the lath morphology and crystallography renders the problem statistically well-posed. As shown in Figure 7, two different cross-sections offer enough information to infer the lath plane normal. Thus, exploiting the sampling of different lath orientations within one observation plane and the assumption of a deterministic relationship between morphology and crystallography, one can identify this relation. This method can be compared to that proposed by Rohrer *et al.* (Rohrer *et al.*, 2004), but, in the present case, the average orientation of a set of discrete interfaces is computed instead of a distribution. Let us emphasize that defining the average orientation based on raw

pixel data, avoids the difficult task of having to tune regularization parameters when extracting boundaries from EBSD maps.

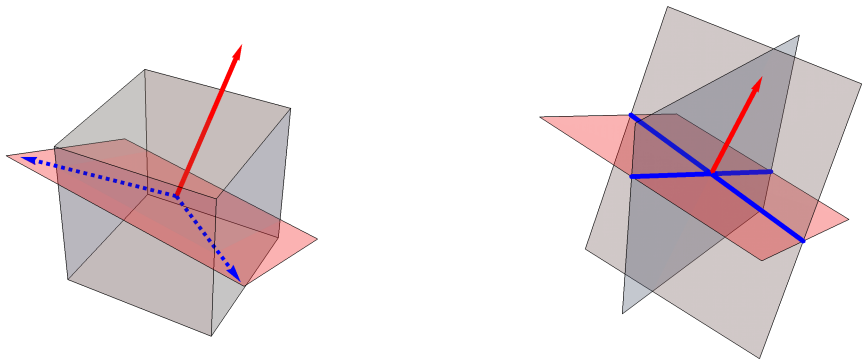

(a) (b)

Fig. 7. Illustration of the geometrical configuration of laths. (a) Illustration of fixed configuration. The lath plane (in red) is fully described by its normal (solid red arrow) or by two non-collinear vectors in the plane (dashed blue arrows). (b) The cross-section by two observation planes (shaded in gray) give laths extended along the blue directions (intersection of lath plane and observation plane). Any cross-section of the lath plane has a principal direction in 2D that is a basis vector of the lath plane in 3D. At least two (non parallel) cross-sections are required to fully determine the 3D lath normal.

The main difficulty of the above identification results from the crystal symmetries and the possible OR variant selection. The proposed methodology is to postulate one possible OR scenario, obtain the most likely lath orientation direction (assigning the closest child variant based on the same variant for each lath packet), and finally check for consistency with the initial postulated OR. Repeating the same approach for all proposed ORs gives a figure of merit to each of them. Hence, an EBSD map can be processed hierarchically to compute

i) the primary ferritic grains,

ii) the child variant clusters inside each primary grain and

iii) the mean morphological orientation with respect to the parent crystallographic

3D frame

However, the mean orientation computation suffers from all the experimental inaccuracies of EBSD maps (definition of phase boundaries according to the imaging technique irrespective of their natural fluctuations). Thus, a large statistical sampling is needed to retrieve the lath normal for each cluster. The pseudo-code for this evaluation of each OR from the measured orientation map is given in Algorithm 4.1.

Require: F ▷ Spatially defined set of α-orientations
Require: A ▷ Spatially defined set of γ-orientations
Require: $\boldsymbol{m}$ ▷ Chosen orientation relationship
$G_f \leftarrow (g_f(n))_{n=1..N_g}$ ▷ Set of N_g grains from F
for $i = 1..N_p$ **do** ▷ Browse the p predicted variants according to $\boldsymbol{m}$
  for $j = 1..N_g$ **do** ▷ Browse every α-grain
    $C_p^m \leftarrow$ Orientations in $g_f(j)$ belonging to the i-th variant cluster according to $\boldsymbol{m}$
    $\boldsymbol{v} \leftarrow$ Mean morphological orientation from C_p^m
    $\boldsymbol{h}(j) \leftarrow$ Corresponding crystallographic orientation of $\boldsymbol{v}$ in parent frame
  end for
  $H(i) \leftarrow$ best perpendicular vector to set $\boldsymbol{h}$
end for

The chosen OR defines the subsets of the orientation map in which the morphological properties are estimated. Each child orientation is attributed to the closest predicted ones considering the local parent orientation and the OR. The mean morphological orientation of each resulting clusters is computed using the structure tensor $\boldsymbol{n} \otimes \boldsymbol{n}$, where $\boldsymbol{n}$ is the mean pixelwise normal vector at the boundary. Its minor eigen vector corresponds to the projection of the mean lath normal in the observation plane while its major eigen vector relates to the direction of extension of the laths in the packet. Likewise, the "best" perpendicular vector to a set of vectors $\boldsymbol{v}$ is conventionally defined as the minor eigen vector of $\boldsymbol{v} \otimes \boldsymbol{v}$.

4.2. Application

The above construction was tested for all "classical" ORs (*i.e.,* B,KS,NW,P,GT). The Pitsch OR appears to provide the most consistent agreement between predicted austenite lath morphology orientation and crystallography. In order to take advantage of a significant statistical distribution, the entire set of acquired maps (140 mm^2) was used to compute the normals of the twelve child variants predicted by the OR. The different steps are illustrated in Figure 8 on the microstructure shown in Figures 2 and 4. Figure 8(a) shows variant clustering of austenite orientations performed in every ferritic grain according to the Pitsch OR (12 variants). The resulting clusters qualitatively encompass a uniform morphological orientation.

The [111] pole figure (Figure 8(b)) reveals how the sampling of child orientations given by the associated variant breaks the continuous distribution (introduced in Figure 3) into discrete clusters. Once the sampling is performed, each variant cluster is processed to compute the principal axis of the laths corresponding to the cross-section between the lath plane and the observation plane (Figure 8(c)). For all processed ferritic grains, this direction is stored as a crystallographic orientation in their frame. Once the sampling is complete, each variant cluster is processed to compute the principal axis of the laths corresponding to the cross-section between the lath plane and the observation plane (Figure 8(c)). These directions should all lie in a plane but some scatter is observed. Laths are not strictly planar and some clusters are not well determined. These differences introduce statistical uncertainties in the principal direction computation. To take into account such errors, the lath plane normal is computed as the "best" (as above defined) perpendicular vector to the set of computed principal directions. As an example, the set of directions and the resulting lath normal for the 12^{th} cluster are shown in Figure 8(d).

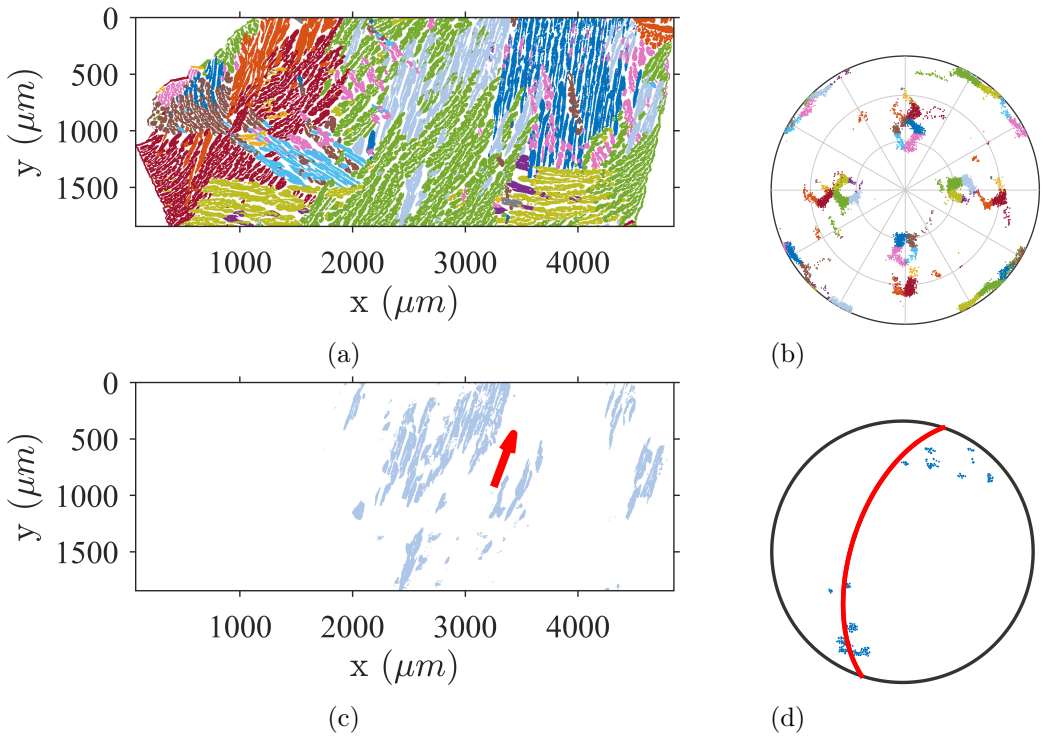

Fig. 8. Illustration of the different steps involved in computing the laths normal for the Pitsch OR. (a) Austenite orientations colored according to their affiliations to the twelve variants given by the Pitsch OR. (b) [111] Pole figure revealing the resulting sampling of the continuous orientation clusters. (c) Principal direction computed from pixels belonging to the 12^{th} cluster. (d) Spherical projection in the parent frame of principal directions for the 12^{th} variant computed in all processed ferritic grains (blue points) and the resulting "mean" plane trace (red line).

The average lath plane pole in the α-frame is given by the direction $\{-0.996, 1.275, 2.366\}_\alpha$ at about 1° from the rational plane $\{\overline{4}, 5, 9\}_\alpha$ and 4.1° apart from the invariant direction $\{\overline{2}, 1, 1\}_\alpha$ given by the Pitsch OR. The proximity with the latter direction is illustrated in Figure 9 by plotting the differences with the computed plane directions and variants of the $\{\overline{2}, 1, 1\}_\alpha$ direction given by Pitsch OR. The standard deviation of the twelve computed poles is 4.45°. This value seems reasonable considering the limited accuracy of trace analysis-based technics on more suitable cases (*e.g.* two planes analysis on sharply defined twin variants yields an accuracy of around 2° at best (Hoekstra, 1980))

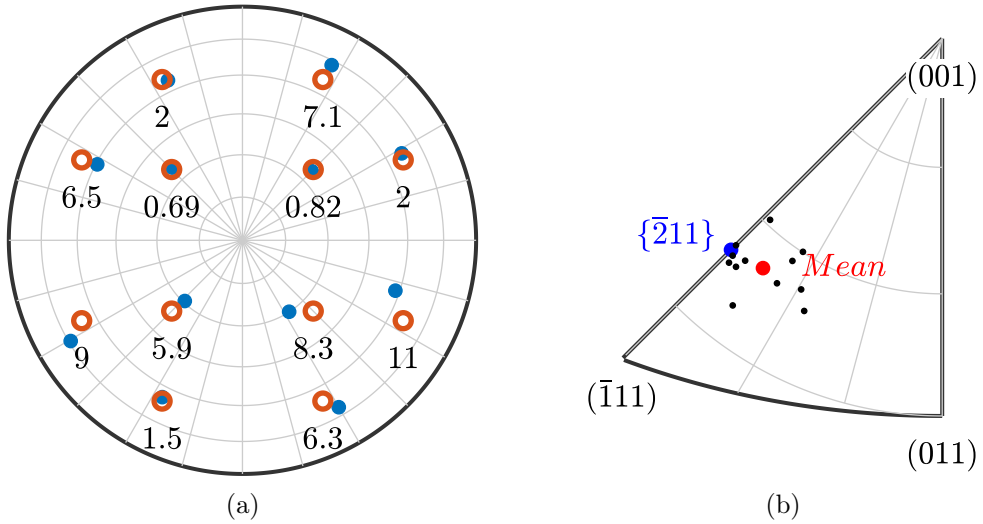

Fig. 9. Comparison between Pitsch invariant direction and computed lath normals in the parent frame. (a) Element-wise variant comparison. The computed directions are plotted as blue points, and $\{\bar{2}11\}$ equivalent directions as red circles. The angular error between both directions is indicated for each variant in degrees. (b) Comparison between the equivalent average pole and direction. The twelve computed poles are represented as black points. The average distance between measured and computed poles is 4.1°

5. Discussion

According to Section 3, the CF8M alloy microstructure in the core of the industrial part is organized hierarchically as follows:

- Large equiaxed ferritic grain network resulting from the liquid to solid phase transformation. Each grain is encapsulated by a thin austenite layer whose orientation lies on the Bain circle of one of the neighboring grains.
- Lath packets that are either distributed on a Bain circle or attributed to an extension of the γ orientation that has grown from prior ferritic grain boundaries. Their morphology is inherited from variant selection or induced crystallographic consistency between the two phases. An appropriate orientation-morphology relationship was found by choosing a Pitsch variant clustering.

- Austenite laths themselves described by their crystal orientation and their affiliations to discrete or smoothly varying position on Bain circles.

The above reading provides a meaningful description of the microstructure from a mechanical point of view. At the observation scale, laths are nearly homogeneous crystals described by their own elasticity and plastic slip directions under mechanical loadings. Lath packets can be modeled by periodic layered domains alternating with two different mechanical responses. The ferritic grains constitute an additional intermediate domain between lath packets and a representative volume that allows one to distinguish packets growing with similar γ-phase orientations on both sides of a prior grain boundary. The mechanical behavior of lath packets is different since the α-phase is oriented differently. Additionally, the lath morphology is most likely different on both sides to accommodate different growing environments. The dedicated workflow to characterize these morphologies is relevant only for orientations belonging to a specific Bain group since it relies on a variant segmentation.

While the method may first appear of poor accuracy, the results appear to be conclusive in the study of CF8M especially considering that it only relies on series of 2D EBSD maps. Interfaces between the two phases at small scales display significant fluctuations and clusters appear in a wide variety of shape with different lath morphologies and spatial configuration. At higher scales, a preferential direction of the laths appears more clearly but is to be measured in a similar manner as the one presented herein. Moreover, the studied slabs are likely to be chemically heterogeneous. Such large ingots exhibit a significant range of cooling rates and high residual stresses are present. Their redistribution during solutionizing combined with diffusion mechanisms add more distortions from theoretically ideal habit planes. They are most likely deformed by the forming process. Figure 10 summarizes the difficulty overcome by the average approach. In most cases, clusters are large enough and characterized with

sufficient details by the EBSD technique to be correctly described with an average definition of the lath normal. This greater part is illustrated in cases (a) and (c) of Figure 10 where the structure tensor gives an admissible normal direction given the visible boundary spread. For these occurrences, the deviation angle between computed normal and $\{211\}_\alpha$ always falls under 5°, which is consistent with the limited accuracy of EBSD analysis. In more ambiguous cases, including heterogeneous data close to primary grain boundaries (Figure 10 (b)) or when the austenite phase appears more globular on the observation plane (Figure 10 (d)), the prediction is less precise but adequately contributes to the mean direction computation of the whole dataset. As a result, the observed gap between theoretical invariant directions and experimentally measured ones is reasonably small (Figure 10) and attributed to experimental deviations of the habit plane and to the out-of-equilibrium configuration due to the long solutionizing treatment.

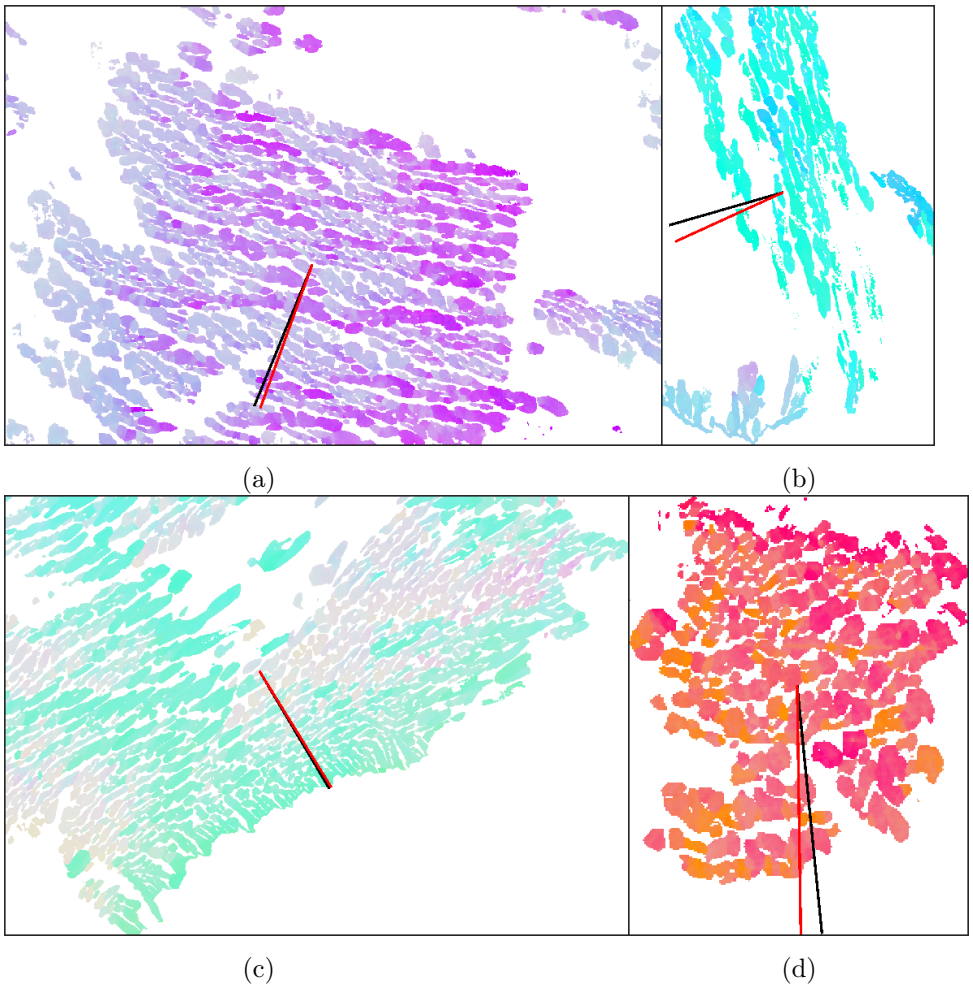

Fig. 10. Examples of lath normal in the observation plane as computed on the image (black lines) and invariant $\{\bar{2}11\}_\alpha$ (red lines) directions in representative clusters. The normals are plotted over IPF-Z maps. The figure illustrates the very small difference between both directions compared to local fluctuations of lath boundaries and the variety of lath cluster morphologies encountered. The angle between both vectors are: (a) 2.37 °, (b) 8.50 °, (c) 0.98 ° and (d) 4.86 °

6. Conclusion

Mappings of child orientations on the specimen space and in the parent crystallographic frame allowed us to investigate the mechanisms of the $\alpha \rightarrow \gamma$ solid to solid phase transformation occurring in the casting process. The inner structure of ferritic grains is mainly composed of austenite lath packets growing from their former bound-

ary. Their growth is constrained by the parent grain volume and simultaneous growth of other packets resulting in a complex layout. It was shown that the lath packets were reasonably segmented according to their distance to Bain OR and to Pitsch OR variants. Some of the packets belonging to distinct Pitsch variants exhibit the particularity of being spatially connected. This effect manifests itself through smooth crystal and morphologic orientation gradients over long characteristic lengths. The morphological orientation was connected to the Pitsch relationship where the child orientation belongs to this OR. A specific method was developed to connect the apparent lath morphology to the local Pitsch variant from the EBSD acquisitions. It enabled for the inference of lath normals in a microstructure with a complex layout. The success of the method proved that austenite lath packets are close to a lath shape. In the present case, it also provided a multiscale segmentation of the microstructure with consistent subsets that are meaningful for understanding the mechanical behavior of the studied dual phase steel. This process required the parent phase orientation map. This step was made easier in the CF8M alloy because of the retained parent phase (Mollens *et al.*, 2022).

The Pitsch OR yielded the best results for the lath properties determination, while it is seldomly cited OR for FCC-BCC systems. Over the set of twelve computed orientations for lath normals, an uncertainty of about $\pm$ 2° was reached. This level was deemed precise enough considering the performance of measurements with precisely defined planes on different materials (Hoekstra *et al.*, 1978; Ameyama *et al.*, 1992). Moreover, multiple factors may lead to a scatter in the locally measured morphology in such large microstructures (*e.g.,* varying thermal gradients, chemical segregation or stress accommodation). Hence, an averaging methodology such as the one conducted herein is desirable.

The present study introduced a segmentation of the microstructure relying on mor-

phological and crystallographic aspects of the two phases. The different scales can be segmented and characterized from EBSD data. In view of the lath morphology, the lath cluster scale suggests that significant anisotropy at near-millimetric scale is to be expected. Each scale is embedded into the one above, but the lath packet scale (between ferritic grain scale and lath scales) has broadly scattered characteristic lengths. Packets also inherit some transversely isotropic properties from the lath morphology. This feature is expected to be of great importance in the distribution of strains inside the material. Otherwise, it would mean that crystallographic effects, such as slip transmission between phases, prevail over morphological ones. The parameters describing lath and lath cluster scales are missing from existing models (Verhaeghe, 1995; Bugat *et al.*, 1999; Mcirdi *et al.*, 2001), and the scale transition rule considered so far does not hold. Instead, the presented results suggest that a sound account of the microstructure at all scales is key to a fair mechanical model. In particular, since aging increases the contrast between phases, such approaches will be needed either to describe plastic flow or to evaluate "hot spots", where stress concentrations will occur and may trigger microvoid or damage ultimately leading to fracture.

Synopsis

Microstructural properties of duplex stainless steel are studied on a wide range of scales using a large EBSD dataset. Image analysis techniques are coupled to crystallographic data analysis to extract relevant features from a complex microstructure.

Acknowledgements

The authors would like to thank EDF (Electricité De France) and ANRT (French National Association for Research and Technology) for their financial support of the PhD of MM.

References

Ameyama, K., Weatherly, G. C. & Aust, K. T. (1992). *Acta Metallurgica et Materialia*, **40**(8), 1835–1846.
https://www.sciencedirect.com/science/article/pii/095671519290170J

Bachmann, F., Hielscher, R. & Schaeben, H. (2010). *Solid State Phenomena*, **160**, 63–68.
https://www.scientific.net/SSP.160.63

Bain, E. C. & Dunkirk, N. Y. (1924). *trans. AIME*, **70**(1), 25–47.

Bate, P. & Hutchinson, B. (2000). *Acta Materialia*, **48**(12), 3183–3192.
https://linkinghub.elsevier.com/retrieve/pii/S1359645400001063

Baur, A. P., Cayron, C. & Logé, R. E. (2019). *Acta Materialia*, **179**, 247–254.
https://linkinghub.elsevier.com/retrieve/pii/S1359645419305336

Bethmont, M., Meyzaud, Y. & Soulat, P. (1996). *Fracture in Austenitic Components*, **65**(3), 221–229.
https://www.sciencedirect.com/science/article/pii/0308016194001334

Bhadeshia, H. (2011). *Scripta Materialia*, **64**, 101–102.

Bouquerel, J., Verbeken, K. & Decooman, B. (2006). *Acta Materialia*, **54**(6), 1443–1456.
https://linkinghub.elsevier.com/retrieve/pii/S1359645405006622

Bugat, S., Besson, J. & Pineau, A. (1999). *Computational Materials Science*, **16**(1-4), 158–166.
https://linkinghub.elsevier.com/retrieve/pii/S0927025699000580

Bunge, H. J., Humbert, M. & Welch, P. I. (1984). *Textures and Microstructures*, **6**(2), 81–95. Publisher: Hindawi.

Bunge, H. J., Weiss, W., Klein, H., Wcislak, L., Garbe, U. & Schneider, J. R. (2003). *Journal of Applied Crystallography*, **36**(1), 137–140.
https://doi.org/10.1107/S0021889802021386

Cai, Y., Shan, M., Cui, Y., Manladan, S., Lv, X., Zhu, L., Sun, D., Wang, T. & Han, J. (2021). *Journal of Alloys and Compounds*, **887**.

Cayron, C., Barcelo, F. & de Carlan, Y. (2010). *Acta Materialia*, **58**(4), 1395–1402.
https://linkinghub.elsevier.com/retrieve/pii/S1359645409007496

Cayron, C., Barcelo, F. & de Carlan, Y. (2011). *Scripta Materialia*, **64**(1), 103–106.
https://www.sciencedirect.com/science/article/pii/S1359646210006123

De Jeer, L., Ocelík, V. & De Hosson, J. (2017). *Microscopy and Microanalysis*, **23**, 1–11.

Engin, C. & Urbassek, H. M. (2008). *Computational Materials Science*, **41**(3), 297–304.
https://www.sciencedirect.com/science/article/pii/S0927025607001073

Fukino, T., Tsurekawa, S. & Morizono, Y. (2011). *Metallurgical and Materials Transactions A*, **42**(3), 587–593.
https://doi.org/10.1007/s11661-010-0285-4

Greninger, A. B. & Troiano, A. R. (1949). *JOM*, **1**(9), 590–598.
http://link.springer.com/10.1007/BF03398900

Haghdadi, N., Cizek, P., Hodgson, P. D., He, Y., Sun, B., Jonas, J. J., Rohrer, G. S. & Beladi, H. (2020). *Journal of Materials Science*, **55**(12), 5322–5339.
http://link.springer.com/10.1007/s10853-020-04358-3

Haghdadi, N., Cizek, P., Hodgson, P. D., Tari, V., Rohrer, G. S. & Beladi, H. (2018). *Philosophical Magazine*, **98**(14), 1284–1306. Publisher: Taylor & Francis _eprint: https://doi.org/10.1080/14786435.2018.1434321.
https://doi.org/10.1080/14786435.2018.1434321

Hansen, N. (2004). *Scripta Materialia*, **51**(8), 801–806.
https://linkinghub.elsevier.com/retrieve/pii/S1359646204003434

Hayashi, T., Morito, S. & Ohba, T. (2020). *Scripta Materialia*, **180**, 1–5.
https://www.sciencedirect.com/science/article/pii/S1359646220300166

He, Y., Godet, S., Jacques, P. J. & Jonas, J. J. (2006). *Acta Materialia*, **54**(5), 1323–1334.
https://linkinghub.elsevier.com/retrieve/pii/S1359645405006750

Hoekstra, S. (1980). *Acta Metallurgica*, **28**(4), 507–517.

Hoekstra, S., Van Der Lelie, H. M. M. & Verbraak, C. A. (1978). *Acta Metallurgica*, **26**(10), 1517–1527.
https://www.sciencedirect.com/science/article/pii/0001616078900627

Jayet-Gendrot, S., Gilles, P. & Migné, C. (2000). *Nuclear Engineering and Design*, **197**, 141–153.

Kim, N. J. & Thomas, G. (1981). *Metallurgical Transactions A*, **12**(3), 483–489.
http://link.springer.com/10.1007/BF02648546

Kurdjumow, G. & Sachs, G. (1930). *Zeitschrift für Physik*, **64**(5-6), 325–343.
http://link.springer.com/10.1007/BF01397346

Le Delliou, P. & Saillet, S. (2015). In *Volume 7: Operations, Applications and Components*, p. V007T07A014. Boston, Massachusetts, USA: American Society of Mechanical Engineers.

Luo, C. & Liu, J. (2006). *Materials Science and Engineering A, Structural Materials: Properties, Microstructure and Processing*, pp. 149–152. Place: Netherlands.
http://inis.iaea.org/search/search.aspx?orig_q=RN:38082287

Maki, T., Tamura, I. & Ameyama, K. (1986). *Japan Institute of Metals, Journal*, **50**, 10–19.

Malik, A., Yeddu, H. K., Amberg, G., Borgenstam, A. & Ågren, J. (2012). *Materials Science and Engineering: A*, **556**, 221–232.
https://linkinghub.elsevier.com/retrieve/pii/S0921509312009276

Mcirdi, L., Baptiste, D., Inal, K., Lebrun, J. L. & Barbier, G. (2001). *Journal of Neutron Research*, **9**(2), 217–225.
http://content.iospress.com/doi/10.1080/10238160108200145

Mollens, M., Roux, S., Hild, F. & Guery, A. (2022). *Journal of Applied Crystallography*, **55**(3), 601–610.
https://scripts.iucr.org/cgi-bin/paper?S1600576722004265

Monlevade, E. F. & Falleiros, I. G. S. (2006). *Metallurgical and Materials Transactions A*, **37**(3), 939–949.
https://doi.org/10.1007/s11661-006-0067-1

Morito, S., Huang, X., Furuhara, T., Maki, T. & Hansen, N. (2006). *Acta Materialia*, **54**(19), 5323–5331.
https://linkinghub.elsevier.com/retrieve/pii/S1359645406005076

Nishiyama, Z. (1934). *Sci. Rep. Tohoku Univ.* **23**, 637.

Nolze, G. (2008). *Crystal Research and Technology*, **43**, 61 – 73.

Nolze, G. & Geist, V. (2004). *Crystal Research and Technology*, **39**(4), 343–352.
https://onlinelibrary.wiley.com/doi/abs/10.1002/crat.200310193

Okamoto, H. & Oka, M. (1992). *Journal of the Japan Institute of Metals*, **56**(11), 1257–1265. 10.2320/jinstmet1952.56.11_1257

Pitsch, W. (1959). *Philosophical Magazine*, **4**(41), 577–584.
http://www.tandfonline.com/doi/abs/10.1080/14786435908238253

Ramachandran, D. C., Kim, S.-D., Moon, J., Lee, C.-H., Chung, J.-H., Biro, E. & Park, Y.-D. (2020). *Materials Letters*, **278**, 128422.
https://linkinghub.elsevier.com/retrieve/pii/S0167577X20311277

Rao, J. C., Ocelík, V., Vainchtein, D., Tang, Z., Liaw, P. K. & Hosson, J. T. M. D. (2016). *Materials Letters*, **176**, 29–32.
https://www.sciencedirect.com/science/article/pii/S0167577X16305663

Rohrer, G. S., Saylor, D. M., Dasher, E. B., Adams, B. L., Rollett, A. D. & Wynblatt, P. (2004). *International Journal of Materials Research*, **95**, 197 – 214.

Self, P., Bhadeshia, H. & Stobbs, W. (1981). *Ultramicroscopy*, **6**(1), 29–40. Publisher: Elsevier Science.

Stanford, N. & Bate, P. (2005). *Acta Materialia*, **53**(3), 859–867.
https://linkinghub.elsevier.com/retrieve/pii/S1359645404006561

Tateyama, S., Shibuta, Y. & Suzuki, T. (2008). *Scripta Materialia*, **59**(9), 971–974.
https://www.sciencedirect.com/science/article/pii/S1359646208005083

Verbeken, K., Barbé, L. & Raabe, D. (2009). *ISIJ International*, **49**(10), 1601–1609.

Verhaeghe, B. (1995). *Étude microstructurale des modes de déformation et de rupture d'un acier austénoferritique vieilli thermiquement*. PhD Thesis. http://www.theses.fr/1995INPG0191

Verma, J. & Taiwade, R. V. (2017). *Journal of Manufacturing Processes*, **25**, 134–152. https://linkinghub.elsevier.com/retrieve/pii/S152661251630158X

Wassermann, G. (1935). **17**, 149–155.

Weatherly, G. C. & Zhang, W. Z. (1994). *Metallurgical and Materials Transactions A*, **25**(9), 1865–1874. https://doi.org/10.1007/BF02649034

Yang, J., Goldstein, J., Michael, J., Kotula, P. & Scott, E. (2010). *Geochimica et Cosmochimica Acta*, **74**, 4493–4506.

Yardley, V. A. & Payton, E. J. (2014). *Materials Science and Technology*, **30**(9), 1125–1130. Publisher: Taylor & Francis _eprint: https://doi.org/10.1179/1743284714Y.0000000572. https://doi.org/10.1179/1743284714Y.0000000572

Zhang, L. H., Cheng, M. J., Shi, X. H., Shuai, J. W. & Zhu, Z. Z. (2021). *RSC Adv.* **11**(5), 3043–3048. Publisher: The Royal Society of Chemistry. http://dx.doi.org/10.1039/D0RA09332G

Zhang, W., Ge, J., Gong, H. & Zhang, X. (1995). *Journal de Physique 4*, **5**(8,pt1), 345–349. Place: France.